A bidirectional bioinspired [FeFe]-hydrogenase model

Md Estak Ahmed, Abhijit Nayek, Alenka Križan, Nathan Coutard, Adina Morozan, Somdatta Ghosh Dey, Reiner Lomoth, Leif Hammarström, Vincent Artero, Abhishek Dey

A Bidirectional Bio-Inspired [FeFe]-Hydrogenase Model

Md Estak Ahmed,[1] Abhijit Nayek,[1] Alenka Križan,[2] Nathan Coutard,[3] Adina Morozan,[3] Somdatta Ghosh Dey,[1] Reiner Lomoth,[2] Leif Hammarström,[2] Vincent Artero,[3,*] Abhishek Dey[1,*]

[1]School of Chemical Sciences, Indian Association for the Cultivation of Science, 2A & 2B Raja S.C. Mullick Road, Jadavpur, Kolkata, India-700032

[2]Department of Chemistry- Ångström Laboratory, Uppsala University, Box 523, SE-75120 Uppsala, Sweden.

[3]Univ. Grenoble Alpes, CNRS, CEA, IRIG, Laboratoire de Chimie et Biologie des Métaux, 17 rue des Martyrs, 38000 Grenoble, France.

Email: vincent.artero@cea.fr, icad@iacs.res.in

Abstract

With the price-competitiveness of solar and wind power, hydrogen technologies may be game changers for a cleaner, defossilized and sustainable energy future. H_2 can indeed be produced in electrolyzers from water, stored for long periods and converted back into power, on demand, in fuel cells. The feasibility of the latter process critically depends on the discovery of cheap and efficient catalysts able to replace platinum group metals at the anode and cathode of fuel cells. Bioinspiration can be key for designing such alternative catalysts. Here we show that a novel class of iron-based catalysts inspired from the active site of [FeFe]-hydrogenase behave as unprecedented bidirectional electrocatalysts for interconverting H_2 and protons efficiently under near-neutral aqueous conditions. Such bio-inspired catalysts have been implemented at the anode of a functional membrane-less H_2/O_2 fuel cell device.

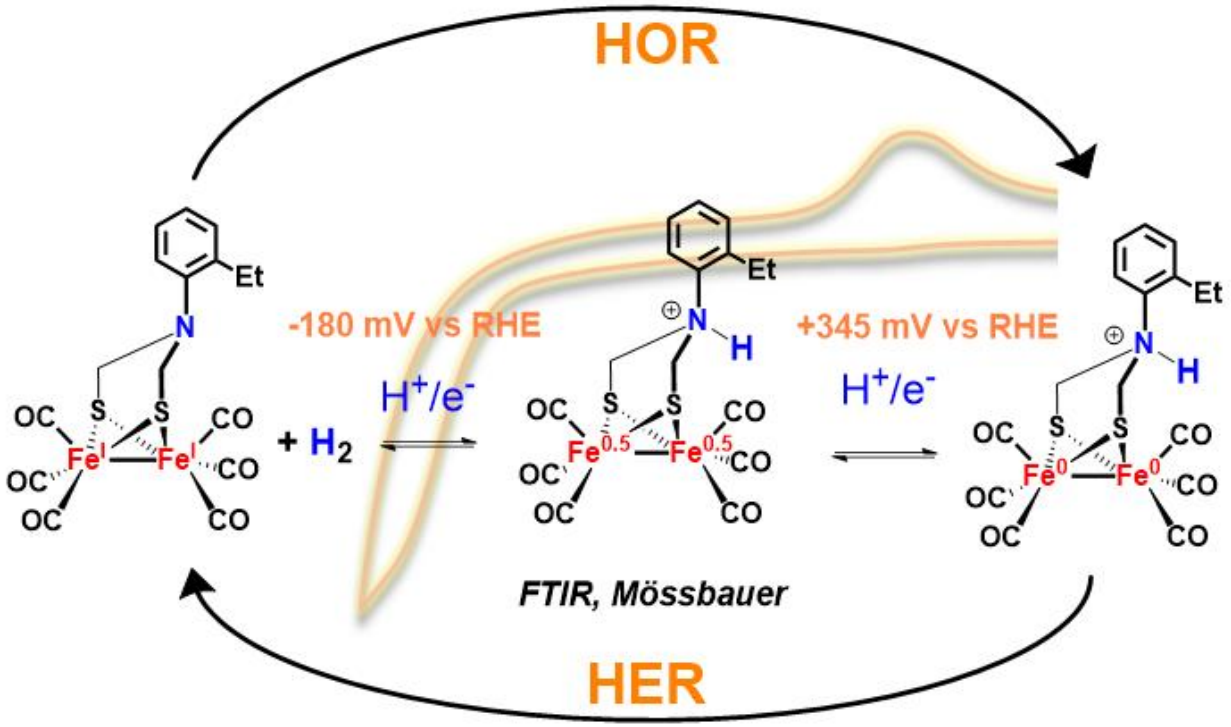

Introduction

Attaining the goal of a clean and sustainable energy cycle is the need of the next decades. Abundant sunlight and water have encouraged the development of a H_2/O_2 based energy cycle. The H_2 and O_2 can be generated from water via electrolysis using sunlight as the source of energy either using solar panel to generate the current needed for electrolysis or by photo(electro)catalysis.[1-9] Similarly, H_2 and O_2 can be combined back in a fuel cell to generate electricity.[10-12] This process, in principle, is sustainable and can have minimum carbon footprint thereby addressing the concern of depleting fossil fuel and the carbon footprint associated with them at the same time. The key to the success of this cycle is the availability of earth abundant metal-based cheap and efficient catalysts for the two half cells involved (Equation i & ii). So far only noble metals have been found suitable as catalysts which has deterred large scale practical implementation of a H_2/O_2 based energy cycle.[13] Apart from the price, the poisoning of the noble metal catalysts by common impurities in H_2O (energy storage) and H_2 (energy release) has concerned energy scientists and technologists attempting to venture in to large-scale solar energy storage applications. In addition, catalyst degradation leads to the leaching of ions that diffuse through the electrolyte, resulting in membrane damages, reducing the lifetime of the whole

system and compromising the recyclability of these expensive catalysts. While biofuel cells using H_2ases[14-18] in membrane-less configuration are demonstrated, these enzymes are degraded by O_2 and inhibited by CO, which are additional barriers against their use under practical conditions.[19-21]

$$\frac{1}{2} H_2 \rightleftharpoons H^+ + e^- \text{ (E = -0.059 V. pH)} \quad \text{(i)}$$

$$\frac{1}{2} O_2 + 2H^+ + 2e^- \rightleftharpoons H_2O \text{ (E = 1.23 – 0.059 V. pH)} \quad \text{(ii)}$$

In the past two decades, there have been substantial developments of catalysts for electrochemical hydrogen generation by electrolysis of acidic-to neutral aqueous electrolytes and several Earth-abundant metal-based catalysts are now known to compete with noble metals for hydrogen generation.[22] Tolerance to oxygen during hydrogen evolution is another issue for practical implementation and some major developments in those directions are already underway.[23-25] On the contrary, noble metal-free alternatives in electrocatalytic hydrogen oxidation is limited to the series of catalysts designed by DuBois and Shaw.[26-29] As far as biomimetic systems are concerned, most mimics of the active site of [FeFe]-hydrogenases models that can activate H_2 only react stoichiometrically in organic solvents[30] and only one[31] has been shown to achieve a few turnovers for H_2 oxidation with ferrocenium used as the oxidant. Therefore, biomimetic electrocatalysis for H_2 oxidation is yet to be achieved. Even more challenging is the discovery of synthetic catalysts able to mediate both H_2 production and oxidation under the same set of experimental conditions. Such bidirectional catalysis has so far only been observed for platinum, hydrogenase enzymes and the above-mentioned DuBois/Shaw catalysts.

We recently developed oxygen tolerant hydrogen evolution [Fe_2] catalysts which are inspired by the binuclear azadithiolato (ADT) bridged active site of [FeFe]-H_2ases (Figure 1).[23] These catalysts are prolific in their application and can be easily integrated with cheap and abundant electrode materials both via adsorption and covalent attachment.[32-34] The [Fe_2] catalysts (see for example complex **1** in Figure 1) differ in their design from previously reported ones in their substitution of the aromatic ring. We observed that inclusion of an alkyl substituent in the *ortho* position of the aryl substitution on the nitrogen bridgehead results in an rotation that suppresses

the delocalization of the amine lone pair into the aromatic ring (Figure 1, bottom).[23] As a result of this loss of electronic delocalization, the basicity of this aliphatic-like amine function increases, allowing its protonation at near neutral pH's, contrary to a *para* substituted/unsubstituted aryl amine (aniline, as in complex **2** in Figure 1) that can only be protonated under quite acidic conditions.[32] A direct consequence of protonation of the nitrogen at higher pH's is catalytic hydrogen evolution at higher pH (i.e. near neutral conditions).[32] Another consequence of the presence of the aromatic *ortho* substituent lies in the change of conformation of the amine function, with the nitrogen lone pair now pointing towards the first coordination sphere of an iron center and allowing for a remarkable resistance to reactive oxygen species and tolerance to O_2 during H_2 evolution.[23,34]

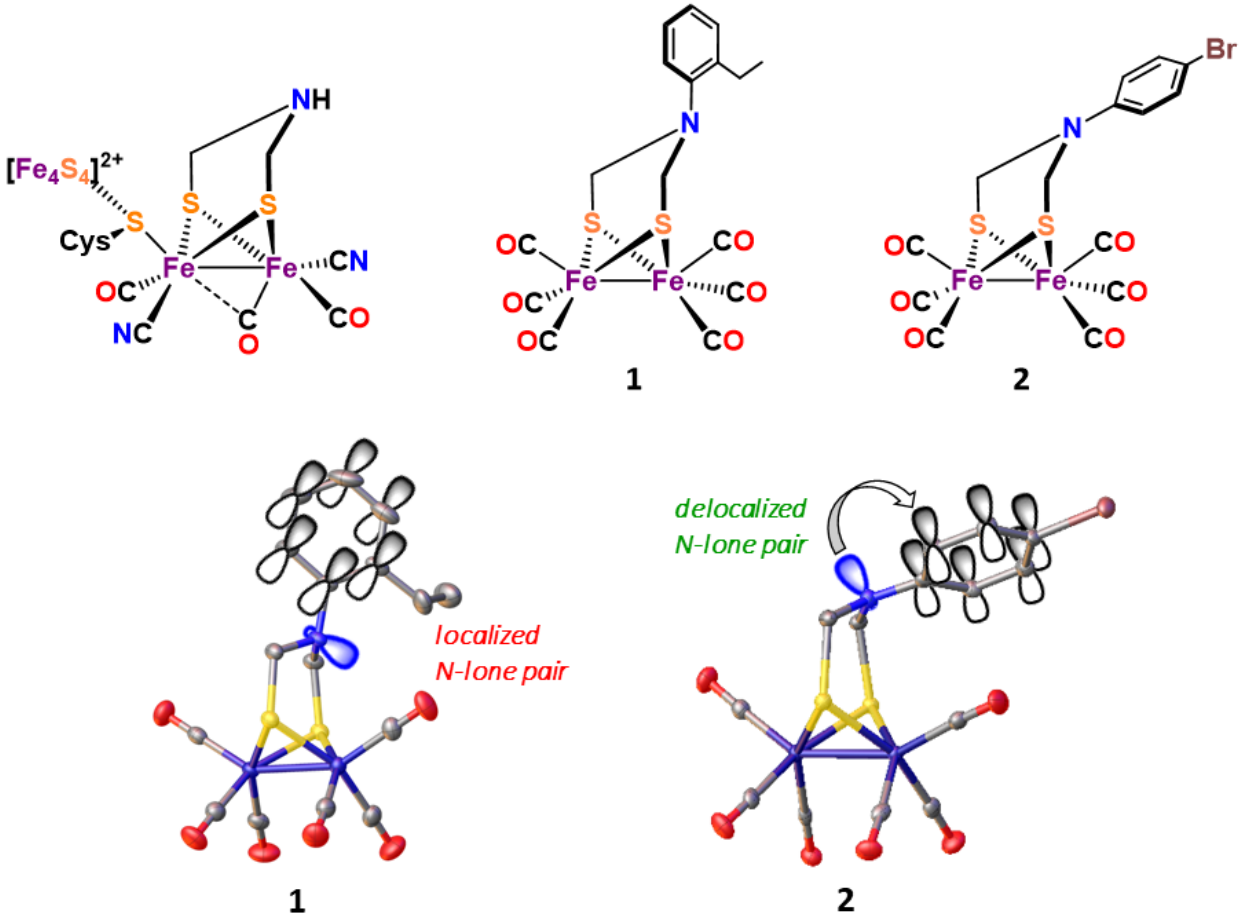

Figure 1. Top: structure of the active site of [FeFe]-H_2ase (H-cluster, H_{ox}) and [Fe_2] subsite mimics **1** and **2**. Bottom: crystal structures of *ortho* (**1**) and *para* (**2**)-substituted complexes showing unfavorable delocalization of the nitrogen lone-pair in **1** due to perpendicular orientation of the planes in the *ortho* substituted complex.

In this report, we show that another feature of such bio-inspired hydrogenase mimics with "rotated" aryl groups is their unique capability to oxidize hydrogen back to proton in both organic and aqueous medium under both homogeneous and heterogeneous conditions, respectively, making them the first series of bidirectional bio-inspired [FeFe]-H_2ase complexes. Their overpotential requirements for electrochemical hydrogen oxidation are moderate (<400 mV) and the large catalytic rate allowed the implementation of catalyst **1** in a membrane-less fuel cell setup with current densities and power densities up to 60 $\mu A \cdot cm^{-2}$ and 31 $\mu W \cdot cm^{-2}$ at 0.6 V cell voltage.

Results

Hydrogen Evolution and Oxidation under Aqueous Conditions

As previously reported, the hydrogen evolution reaction (HER) is catalyzed by **1** adsorbed on edge plane graphite (EPG) electrode from water, thus under heterogeneous conditions, at near neutral pH (pH 5.5) with mild overpotential requirements (160-180 mV, Figure 2a).[23] The enhanced basicity of the nitrogen lone pair can also be advantageous for the hydrogen oxidation reaction (HOR) as it can facilitate the heterolysis of the H–H bond by stabilizing the incipient proton, leaving a hydride bound to the Fe_2S_2 cluster. Indeed, when the **1**-modified EPG electrode is swept at potential negative enough for H_2 evolution to occur (Figure 2a, green and blue lines), a peak at 525 mV vs RHE is observed in the return anodic scan. Note that the solution does not contain any added H_2 to begin with. This signal is not observed if the cathodic scan is stopped before the HER process (Figure 2a, orange line). This anodic peak also appears when anodic linear sweeps are performed after bulk electrolysis has been performed at –475 mV vs RHE to produce H_2 (Figure 2b, red line). The intensity of the oxidation peak increases with increased

electrolysis time (Figure 2b, inset), i.e. as the concentration of H_2 in the solution increases. These data are suggestive of HOR by complex **1** of the H_2 generated *in-situ* by HER by the same complex. The HOR current is not observed when the electrode is rotated (Figure 2b, purple line) as the generated H_2 flows away from the electrode upon rotation. Finally, hydrogen oxidation was confirmed by monitoring the HOR current at 425 mV vs RHE under various partial pressures of H_2 in H_2/N_2 mixtures (Figure 2c) with the HOR current increasing linearly with H_2 partial pressure (Figure 2d) as is expected for heterogeneous electrocatalysis where the substrate diffuses from bulk solution.[34]. The HOR current is not observed in complex **2** which does not have the *o*-substituent implying that the delocalization of the bridgehead nitrogen lone pair into the ring makes it unable to activate H_2 (Figure S2). For heterogeneous electrocatalysis, the I_{cat}/I_p ratio is the direct measure of the turnover frequency at saturation (TOF_{max}). It is a convenient way of defining the catalytic efficiency of a heterogeneous electrocatalysts. The TOF_{max} of complex **1** for H_2 oxidation is calculated to be ~ 1.6 s^{-1} under 1 atm. of H_2. To check the stability of complex **1** long-term controlled potential electrolysis (CPE) has been carried out. The stable electrolysis current (Figure S3) implies that the catalyst is stable even after 11 h of electrolysis under catalytic conditions. Moreover, ATR-FTIR of complex **1** physisorbed on EPG surface, before and after controlled potential electrolysis shows that the complex is stable even after a few hours of electrolysis (Figure S4).

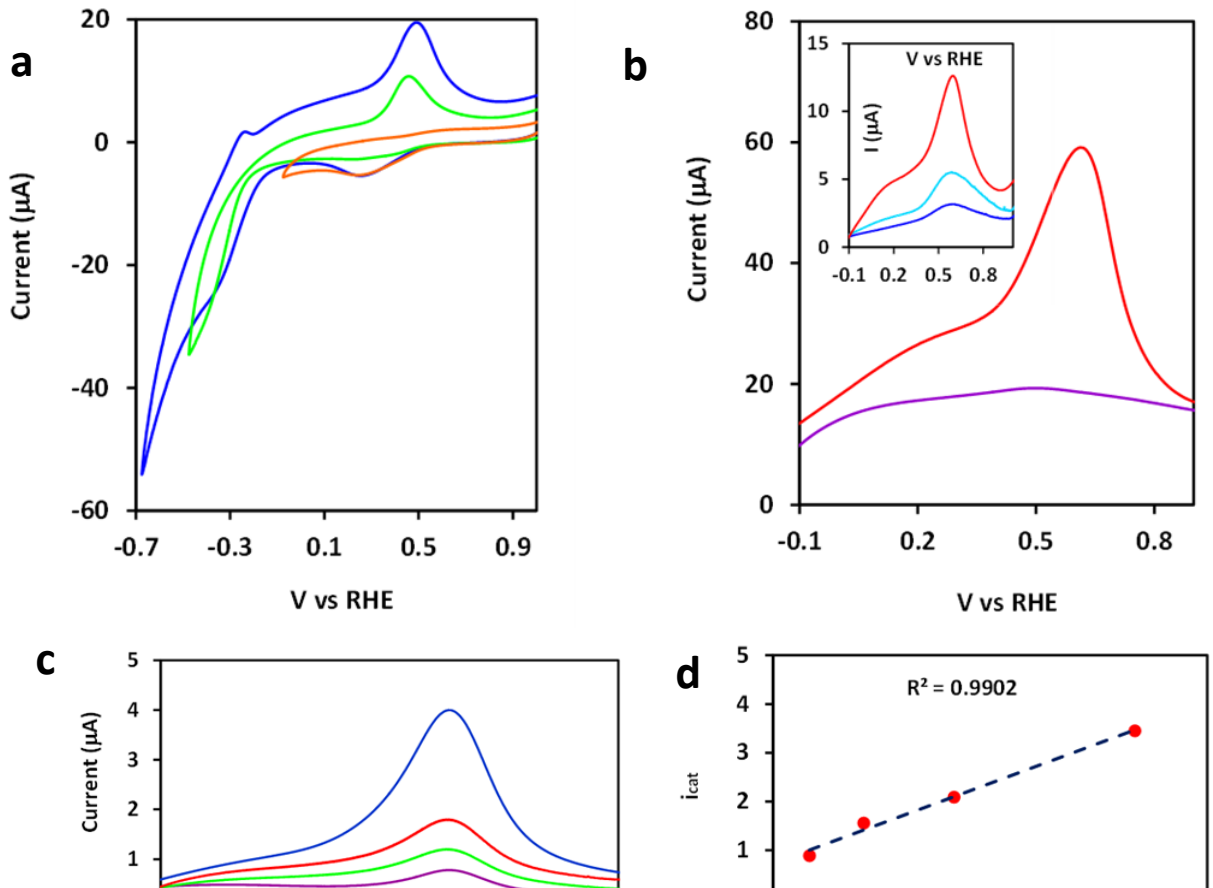

Figure 2. Electrochemical data for **1** physisorbed on EPG surface in 0.1 M aq. KPF_6 solution (i.e. under heterogenous conditions, pH = 5.5): (**a**) Overlay of CV data at different potential ranges; (**b**) Linear sweep voltammetry taken from -0.1 V to 0.9 V vs RHE directly after (red) 210 s bulk electrolysis at –0.475 V vs RHE and then (purple) after few minutes of rotation at 600 rpm in the same solution; *inset*: Linear sweep voltammetry after different times (60s, 120s, and 180s) of controlled potential electrolysis at –0.475 V vs RHE; 60s (navy blue), 120s (sky blue), 180s (red), scan rate: 100 mVs^{-1}; (**c**) Linear sweep voltammetry taken from 0.0 V to 0.7 V vs RHE at different H_2 partial pressures; no H_2 (black), 10% H_2 (purple), 25% H_2 (green), 50% H_2 (red), and 100% H_2 (blue), scan rate: 100 mVs^{-1}; (**d**) plot of i_{cat} vs partial pressure of H_2, where i_{cat} is the catalytic current measured at 0.425 V vs RHE in Figure 2c.

Hydrogen Oxidation in Organic Solvents

To experimentally confirm HOR and determine the faradic efficiency of this process, we shifted to homogeneous non-aqueous conditions. These conditions allow us to quantify the formation of protons, i.e., the products of H_2 oxidation by capturing them with a well-defined base such as N,N-diisopropylethylamine (*i*-Pr_2NEt). The cyclic voltammetry of a 1 mM solution of complex **1** in CH_3CN solution under 1 atm of H_2 in the presence of *i*-Pr_2NEt (5 mM) shows an anodic catalytic oxidation which increases with the addition of *i*-Pr_2NEt (Figure 3a) suggestive of electrochemical oxidation of H_2 by complex **1**. The current increases linearly with square root of partial pressure of H_2 (Figure 3b & 3b, inset) consistent with a 1st order dependence of the homogeneous catalytic process on H_2.[35,36] The electrocatalytic HOR process mediated by **1** has a half peak potential of −750 mV vs $Fc^{+/0}$. The apparent standard potential of H_2 oxidation in CH_3CN is –1.14 V vs $Fc^{+/0}$ using 18.1 as the pKa value of *i*-Pr_2NEt in acetonitrile[37] and –0.07 V vs $Fc^{+/0}$ as the thermodynamic proton reduction potential value.[27,38] This indicates that the overpotential (electrochemical driving force) requirement for HOR catalyzed by complex **1** is ~400 mV in acetonitrile solution. This value compares well with the HOR overpotential requirement displayed in acetonitrile by most DuBois' catalysts.[29,39-42] The proton generated

from oxidation of H_2 is converted to *i*-Pr_2NEtH^+ cation. Quantification of the *i*-Pr_2NEtH^+ cation by ^1H NMR during the course of a bulk electrolysis (BE) experiment carried out in 0.5 mM CD_3CN solution (6 ml) of the catalyst in presence of large excess of *i*-Pr_2NEt (10 M) at –0.7 V vs $Fc^{+/0}$ under 1 atm of hydrogen (charge passed = 136 C over 10 h) shows the gradual depletion of the signal corresponding to H_2 at 4.57 ppm and growth in the signal corresponding to *i*-Pr_2NEtH^+ at 7.59 ppm (Figure 3c). There is no appreciable decay (only 6%) or change in the UV-visible spectra before and after long term BE experiments of the complex indicating that this complex is quite stable under these conditions (Figure S5). Quantification of the *i*-Pr_2NEtH^+ signal and its ratio with the charge consumed yields the FY to be 82 ± 3% (Table S1). The turnover number (TON) after 10 h of electrolysis ranges between 192 and 204 (taking into account a 6% decay of the catalyst during the reaction). No HOR is observed for complex **2** under the same conditions commensurate with the proposal that the basicity of the bridgehead nitrogen is key to H-H heterolysis (Figure S6).

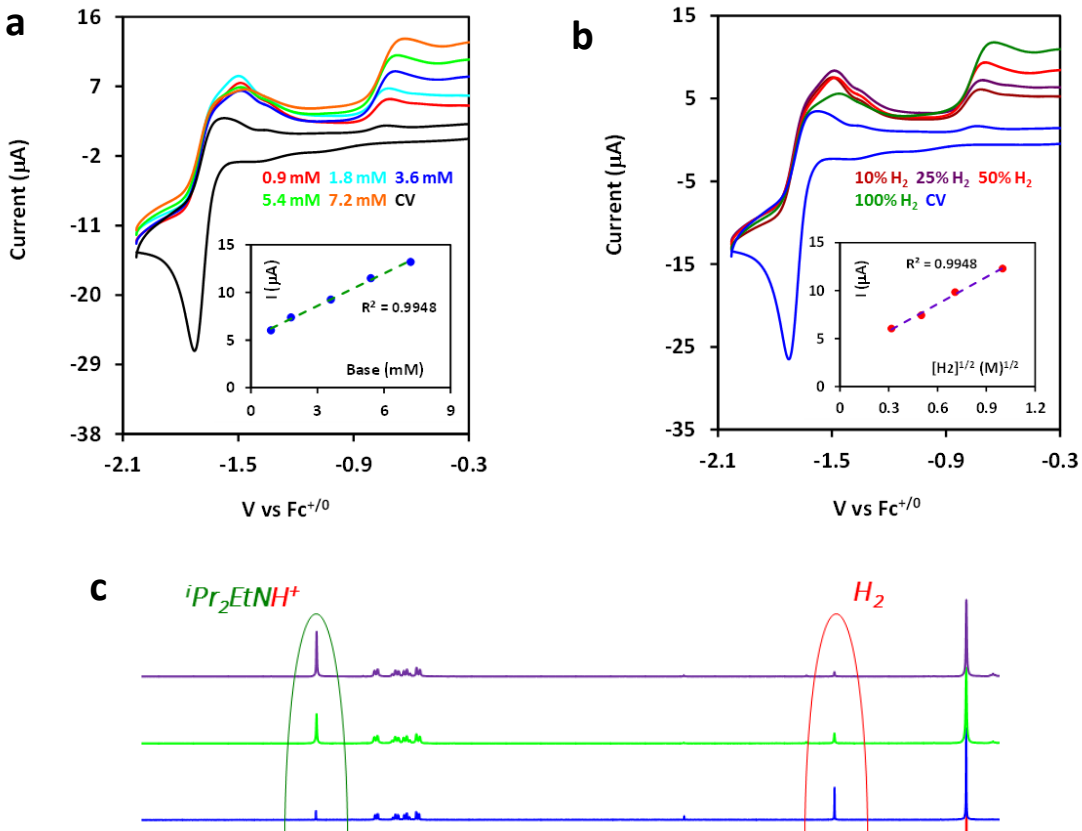

Figure 3. Electrochemical data for **1** in acetonitrile medium under homogeneous conditions. (a) Cyclic voltammetry of **1** in acetonitrile and Linear sweep voltammetry in the presence of different concentration of base; (*inset*) Peak current vs concentration of base plot. (b) Linear sweep voltammetry of **1** in acetonitrile at different H_2 concentrations in presence of 5 mM *i*-Pr_2NEt (scan rate: 100 mV s^{-1}). (*inset*) Peak current vs square root of partial pressure of H_2 plot (c) ^1H NMR of complex **1** in CD_3CN after different time of bulk electrolysis; initial (black line), 40 min (yellow line), 90 min (red line), 140 min (blue line), 250 min (green line), and 420 min (purple line), in the presence of large excess (10 M) of *i*-Pr_2NEt.

Time-resolved FTIR Spectroscopy

Rapid scan FTIR spectroscopy was employed to investigate the mechanism of HER catalysis by complex **1**. FTIR spectroscopy is a useful tool for discerning changes in the electronic density on metal carbonyls due to the sensitivity of the carbonyl peaks to their electronic environment. As both reduction and protonation alter the electronic density on the diiron core, the carbonyl peaks could be used to gain information on the electronic and protonation state of complex **1**.

An acetonitrile solution containing complex **1** and excess $CoCp_2$ (electron source) was rapidly mixed with excess malonic acid (proton source, pKa = 15 in acetonitrile) using a stopped flow mixing table and monitored using FTIR spectroscopy (Figure 4). The earliest recorded spectrum (< 8 ms) showed three pronounced peaks (2076, 2038 and 1998 cm^{-1}) which correspond to those of the resting complex **1** in the Fe(I)Fe(I) state. As more time elapsed, these three peaks disappeared and four new peaks appeared at 2028, 1975, 1930 and 1885 cm^{-1}. No major differences could be observed between the IR spectra recorded at 2 min and 50 min, suggesting species **1** was rapidly and quantitatively converted to another long-lived species. This newly

formed species had its carbonyl peaks red shifted by 50-70 cm^{-1} with respect to **1**, as well as an additional, forth peak at 1885 cm^{-1}. The shift to the lower wavenumbers implied reduction of the diiron core. The shift magnitude was in good agreement with a shift expected for a Fe(0)Fe(I) core. A similar spectrum had already been experimentally observed for another diiron azadithiolate complex by Aster et al.[43] The N-protonated, singly reduced form of their diiron azadithiolate complex had its carbonyl peaks at 1880, 1935, 19600 and 2020 cm^{-1} (Table 1).[43] Similarities between the two spectra, i.e., the magnitude of the peak shift upon reduction as well as the number of carbonyl peaks suggested that the long-lived species could be the N-protonated, singly reduced species **1H** (scheme 1).

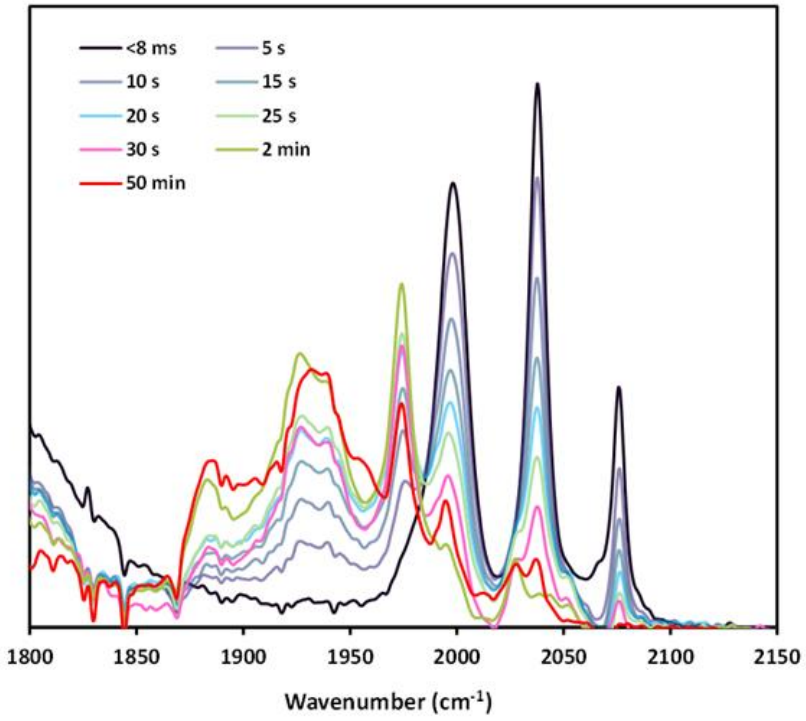

Figure 4. Time-resolved FTIR spectra recorded after the rapid mixing of the complex **1**, $CoCp_2$ and malonic acid. Times indicated in the legend are relative to the rapid mixing event.

Chemical Synthesis and Spectroscopic Characterization

FTIR

As **1H** was found reasonably stable during time-resolved FTIR measurements, we decided to chemically synthesize the same intermediate. To achieve this, the complex **1** was chemically

reduced by excess cobaltocene ($CoCp_2$) in the presence of malonic acid. The resulting FTIR spectrum (Figure 5a) shows that the characteristic bands of complex **1** at 2076, 2038, and 1998 cm^{-1} disappears and instead three new bands appear at 2028, 1975 and 1930 cm^{-1}. These

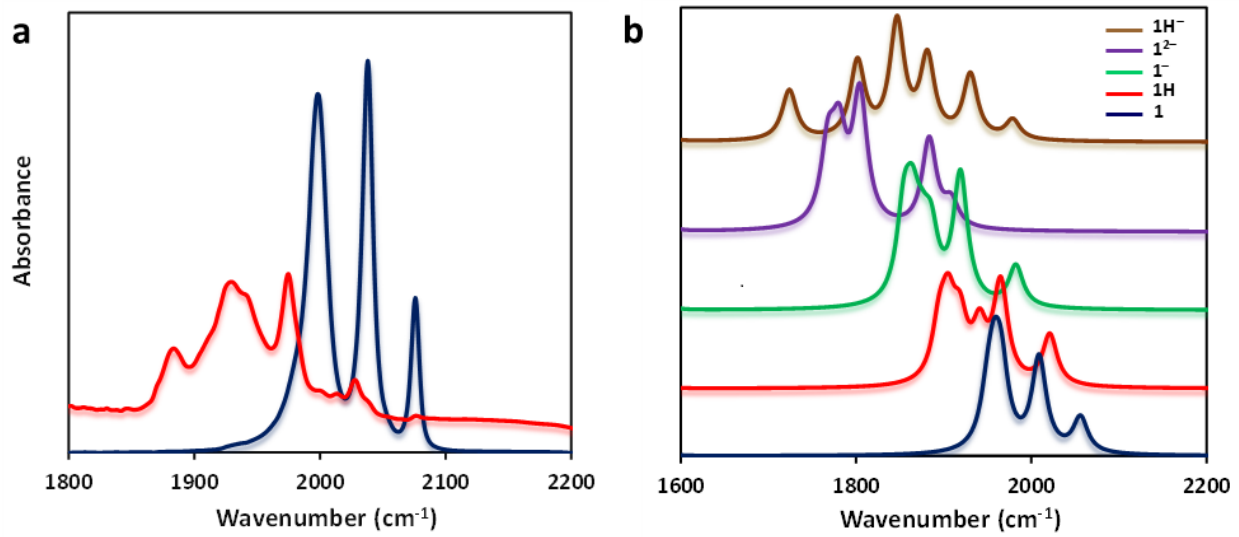

vibrations are identical to those obtained in the time-resolved FTIR data in Figure 4. The magnitude of the peak shifts compared to the starting material **1** is almost identical to those observed for the singly reduced and N-protonated adt-bridged complexs.[43,44] DFT calculations are used to gauge the shifts in FTIR spectrum associated with reduction of **1** (blue) to $\mathbf{1}^{-}$ (green) and $\mathbf{1}^{2-}$ (purple) and the corresponding protonated species **1H** (red) and $\mathbf{1H}^{-}$ (brown) (Figure 5b). The DFT computed FTIR data of both **1** and **1H** agree reasonably well with that of the experimental data (Figure 5a).

Figure 5. (a) FTIR data of complex **1** (navy trace) and chemically synthesized **1H (**red trace) in acetonitrile medium. (b) DFT optimized FTIR data of complex **1** calculated in various redox and protonation states.

Table 1. CO Stretching frequencies

	Experimental IR stretching frequencies of complex 1 (cm^{-1})	**Previously reported IR stretching frequencies of an adt complex.[43]**
1	1998,2038,2076	1994, 2034, 2075
1H	1885, 1930, 1975, 2028	1890, 1935, 1960, 2020

Mössbauer spectroscopy

To obtain further information on the structure of and the redox state of the two iron centers, Mössbauer spectrum was recorded at 90 K for both the complexes **1** and **1H** and summarizes the data in Table 2. The Mössbauer spectrum of parent complex **1** shows one doublet with isomer shift δ_{iso} = −0.065 ± 0.01 mm.s^{-1} and quadrupole splitting ΔE_Q = 0.83 ± 0.01 mm.s^{-1} (relative to α_{Fe}) (Figure 6a) attributed to the two identical Fe(I) centers in its butterfly Fe_2S_2 cluster core. These values are in agreement with those obtained for the structurally related diiron complex [$Fe_2(\mu$-$SCH_2OCH_2S)(CO)_6$] (IS, δ_{iso} = −0.02 mm.s^{-1} ; QS, ΔE_Q = 0.81 mm.s^{-1} (relative to α_{Fe}).[45,46] The Mössbauer data of **1H** (one electron reduced protonated species), on the other hand, exhibits a quadrupole doublet with an isomer shift δ_{iso} = −0.049 ± 0.01 mm.s^{-1} relative to α_{Fe} and a quadrupole splitting ΔE_Q = 0.79 ± 0.02 mm.s^{-1} (Figure 6b), which implies the two Fe centers in **1H** is identical as well. Thus, the electronic structure of the **1H** species is best described as Fe(0.5)Fe(0.5), consistent with the fact that the LUMO is a Fe-Fe σ* orbital and addition of 1e$^-$ to this orbital results in a delocalized mixed-valent Fe(0.5)Fe(0.5) state. The X-band EPR of **1H** at 77 K shows a rhombic signal with g_x = 2.07, g_y = 2.06, and g_z = 1.99 (Figure S7) consistent with an S = 1/2 overall spin state.

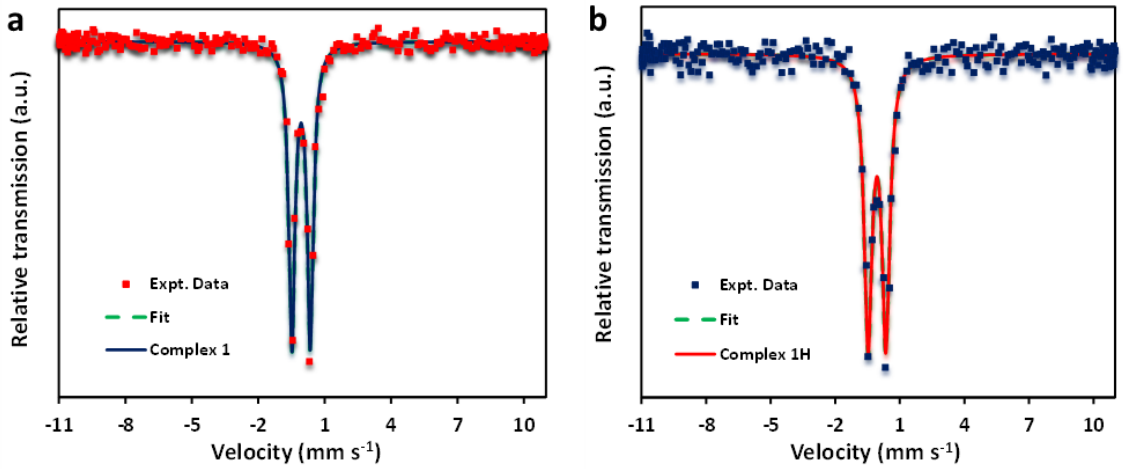

Figure 6. Mössbauer spectra of (a) **1** and (b) **1H** recorded at 90 K.

Table 2. Experimental Mössbauer data recorded at 90 K

Mössbauer parameters	Complex 1	Complex 1H
δ_{iso} (mm s^{-1})	-0.065 ± 0.01	-0.049 ± 0.01
ΔE_Q (mm s^{-1})	0.83 ± 0.01	0.79 ± 0.02

Proposed Mechanism

Complex **1** can produce as well as oxidize hydrogen, thus reproducing a unique characteristic of the active sites of natural hydrogenases. Complex **2** does not show HOR at all but exhibits HER activity in highly acidic solutions. Hydrogenases can perform both conversions generally without any substantial overpotential requirement, contrary to the complex observed here that exhibit bidirectional activity but with overpotential requirement for both processes. Of note, a putative sensory [FeFe]-hydrogenase enzyme has been recently described with a unique bidirectional irreversible behavior quite similar to the activity reported here for complex **1**,[17,18] catalyzing HER with an overpotential requirement of 180 mV and HOR with an overpotential requirement of 400 mV, both measured at the onset of the catalytic waves in aqueous medium under heterogeneous conditions). The first redox process observed for **1** (Fe(I)Fe(I) state) is found around 345 mV vs RHE and shifts by 50 mV per pH unit towards positive potential, indicating that the first reduction of **1** is accompanied by protonation to form the Fe(0.5)Fe(0.5)-NH species **1H**, which could be isolated and characterized as described above. Note that the HER mechanism for these complexes in organic medium are different.[47] Sweeping to more negative potentials, position of inflexion of HER potential is then shifted by 57 mV/ pH unit (Figure S8), suggesting that the second reduction process is also coupled to protonation resulting in H_2 evolution catalysis and regeneration of **1**, which immediately equilibrates with the electrode and the solution to form **1H** in the Fe(0.5)Fe(0.5)-NH resting state. **1H** is however unable to activate H_2 so that HOR activity is only observed at more positive potentials, where **1** is the predominant species. Actually, **1H** is an intermediate in both HER and HOR (see below) processes but is inert toward both protons and H_2 substrates. **1H** predominates between +425 mV and –275 mV vs RHE and hence no catalysis is observed in this potential window, explaining the irreversible behavior. By contrast, the two consecutive reduction of the 2Fe active site and the proximal Fe_4S_4 cubane occur at similar potentials in reversible hydrogenases.[21]

To gain additional insights into H_2 activation, a theoretical gauging of the mechanism (G16[48], B3LYP functional[49,50], 6-311+g* basis set, PCM-dispersion model) was undertaken. The same method has allowed accurate prediction of the vibrational properties of a wide range of binuclear hexacarbonyl model complexes of hydrogenases.[51] It revealed that the rotation of a CO ligand

from a terminal to a bridging position in the Fe(I)Fe(I) state of complex **1** allows binding of H_2 in a side-on manner (Scheme 1 & Figure S9, top). Then H–H heterolysis can proceed resulting in a terminal iron hydride and anilinium proton, which are di-hydrogen bonded to each other. The calculated total free energies of these reactions (product – reactant) indicate that the H_2 binding energy is ~23.5 kcal mol^{-1}. The experimentally determined rate of H_2 oxidation is ~1.6 s^{-1}, which is consistent with the large endothermicity of the rate-determining H_2 binding step. Similar calculations with complex **2** show that the H_2 does not bind the open site in the rotated μ-CO structure as the phenyl substituent, in plane with the bridging nitrogen, rests on top of the open co-ordination site on the iron, sterically hindering H_2 binding to the cluster (Figure S9, bottom).

Taken together and combined with the current mechanistic knowledge for this class of complexes regarding HER,[52,53] these data allow us to propose in Scheme 1 a consistent mechanism for HER and HOR catalyzed by **1**. The two consecutive PCET steps involved in HER from the Fe(I)Fe(I) state finds support in the 50-59 mV/pH dependence of both the first reduction wave and the second catalytic wave in aqueous medium as well as in the isolation of **1H**. The second PCET reduction of **1H** is the rate-determining step during HER as suggested by its isolation when excess reducing agent and a weak acid is added to the Fe(I)Fe(I) state. The H_2 binding to **1** is very endothermic whereas the H–H bond formation from the $2e^-/2H^+$ reduced Fe(0)Fe(2)-H;NH state is strongly exothermic (with no barrier for proton binding), which likely explains the catalytic bias towards HER over HOR observed for **1**.

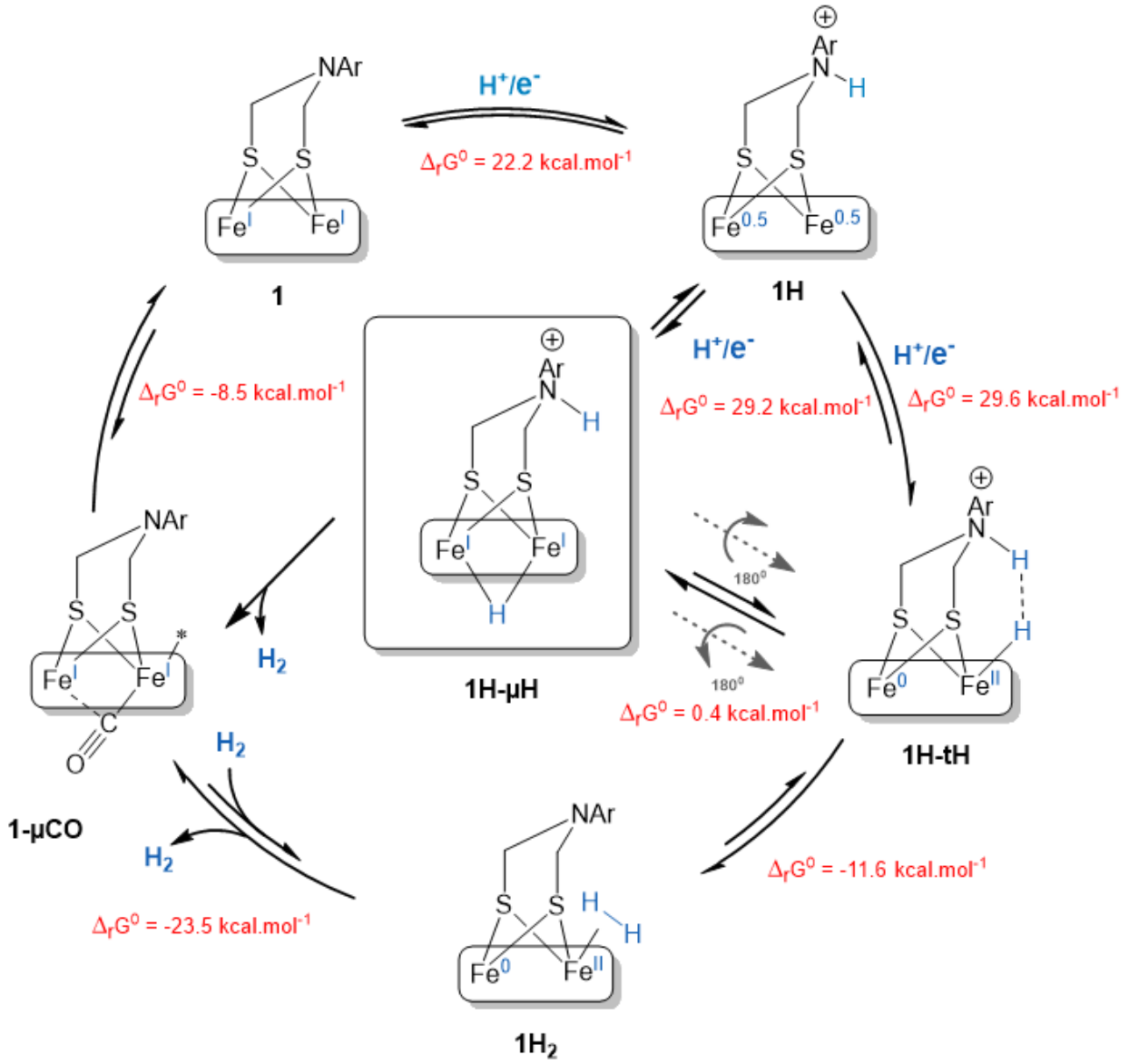

Scheme 1. Proposed mechanistic cycle(s) for HER and HOR catalyzed by heterogenized complex **1** in aqueous electrolyte, including a HER route via bridged hybride intermediate. Computed E^0 and Δ_rG^0 values are indicated.[54]

We include in Scheme 1 the isomerization between terminal and bridging hydride derivative which is found quasi thermo-neutral. This is at variance with classical [Fe2] mimics for which the bridging form is significantly more stable and constitute the natural route for HER catalyzed by **2**. In addition, the impossibility for the ammonium proton to be positioned close to the transient terminal hydride ligand [55] make HER through intramolecular proton-hydride coupling unlikely for **2**. Still, the involvement of **1H-μH** intermediate cannot be ruled out for

intermolecular H_2 evolution, depending on the experimental conditions, or as intermediate between **1H-tH** and **1H** in intramolecular processes.

1 activates H_2 in its formal Fe(I)Fe(I) states (Scheme 1). By contrast, both the active site of classical [FeFe]-hydrogenases (Scheme 1)[21,40-42] and the ferrocene-bearing diiron mimic ($FcFe_2$) reported by Rauchfuss and coworkers[31] react with H_2 in the Fe(II)Fe(I) state. Such a deviation of the reactivity relative to electronic structure is due to the difference in the ligand environments in these systems. In the natural active site, a CN^- ligand and a thioether ligand replaces two π-acid CO ligands in complex **1**, resulting in increased electron density of the diiron cluster. The same is true for the $FcFe_2$ complex where the diphosphine ligand replaces the two π-acid CO ligands in **1**. This is why the Fe(II)Fe(I) mixed valent state is required to oxidize H_2 in the enzyme active site and $FcFe_2$ complex while the Fe(I)Fe(I) state of complex **1** can react with H_2. Of note, this increased electron density in the active site also makes hydrogenases able to evolve H_2 from a Fe(I)-Fe(II)-H_2 state,[56-59] which is more oxidized by one redox equivalent than the Fe(I)-Fe(I)-H_2 state required for **1** to cycle.

Of note, the mechanism observed for the complex in non-aqueous conditions depends on whether reduction/oxidation is achieved chemically or electrochemically. While $\mathbf{1}^-$ and **1H** are observed when Cp_2Co is used as the reductant, these species are not observed during electrochemical reduction (Figure S10, see also the comment in the Supporting Information). Therefore, the bidirectional mechanism observed for the adsorbed complex in aqueous conditions is at variance with that occurring at the vicinity of an electrode in non-aqueous, and homogeneous, conditions in the presence of mild proton sources such as malonic acid and/or mild bases such as *i*-Pr_2NEt. Under these conditions, HER proceeds directly from the Fe(0)Fe(0) state (Figure S10); Similarly, we posit that the **1H** species produced from HOR rapidly disproportionate to generate **1** and protonated forms of $\mathbf{1}^{2-}$. This discrepancy between catalytic behaviors for HER/HOR is reminiscent for that of the initial series of DuBois complexes, which displayed various reactivity when solubilized in acetonitrile[47] or adsorbed on electrode and assayed in acidic aqueous conditions.[60]

HOR in a membrane-less fuel cell setup

The good catalytic performance measured for H_2 oxidation of complex **1/EPG** electrodes in mildly acidic solution prompted us to integrate them in H_2/O_2 fuel cell devices. As **1** is active in

near neutral aqueous environment (pH 5.6) and cannot withstand the highly acidic conditions required for implementation in Proton-Exchange Membrane (PEM) fuel cells, we turned to a membrane-less fuel cell architectures that has been developed for biocatalysts and other bio-inspired catalysts. The selectivity of these (bio)catalysts makes them unsensitive to potential substrate crossover, which allows saving the cost of membrane. Instead a liquid electrolyte is used. To that end, we prepared gas diffusion electrodes (GDEs) circumventing solution H_2 mass-transport limitation. Commercial Sigracet gas diffusion layer (GDL) substrates covered with a microporous layer were drop-casted with an ink based on the complex **1**, carbon black and CH_2Cl_2. Best results were found with a carbon black/complex **1** mass ratio of 2 corresponding to a loading of 60 nmol.cm^{-2}. These GDEs were first assessed under a back flow of H_2 at atmospheric pressure in three-electrode half-cell configuration (see SI), as previously described,[60,61] using a 0.1 M KPF_6 aqueous electrolyte (pH 5.6). Figure 7 shows the typical cyclic voltammograms recorded under these conditions, confirming the property of the heterogenized complex **1** to catalytically oxidize H_2 with onset overpotential requirement of ~0.2 V and current densities reaching 0.4 mA.cm^{-2} at 0.8 V overpotential. For comparison, the polarization curve recorded on a commercial Pt/C electrode (0.5 mg_{Pt}.cm^{-2}) is also shown on Figure 7. Noteworthy, the Pt loading (2.5 10^{-6} mol_{Pt} cm^{-2}) is ~20 fold higher than that of iron (1.2 10^{-7} mol_{Fe} cm^{-2}). Figure S11 shows that both electrodes display specific catalytic current density (expressed in A mol_M cm^{-2}) in the same range.

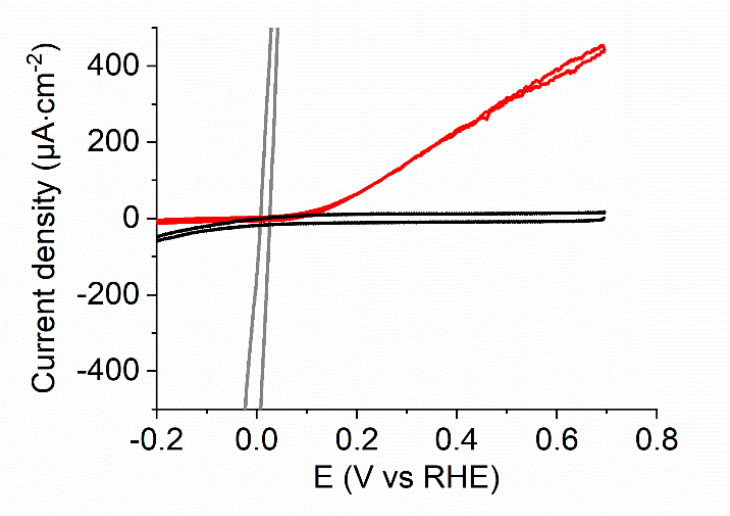

Figure 7. CV of a complex **1**/carbon black GDE (carbon black/ complex **1** mass ratio of 2, 60 $nmol_{complex\ \mathbf{1}}.cm^{-2}$) (red solid line), a carbon black GDE (black solid line) and of a conventional Pt/C (0.5 $mg_{Pt}.cm^{-2}$) GDE (grey solid line) in 0.1 M aqueous KPF_6 pH = 5.6 adjusted with HCl and under back-flow H_2 (1 atm H_2, S = 0.38 cm^2, ν = 10 mV s^{-1}, 20°C).

The complex 1/carbon black GDEs were then integrated in the above mentioned unconventional membrane-less H_2/O_2 fuel cell setup using continuously degassed 0.1 M KPF_6 electrolyte adapted from our previous report[62,63] and operated at 25°C. The complex 1-based anode was coupled with a cathode based on a commercial 0.5 $mg_{Pt}.cm^{-2}$ GDE installed in a second electrode holder fed with pure O_2 at atmospheric pressure (Figure S12). GDEs used in this setup allow each catalyst to work at the interface between the electrode, the liquid electrolyte ensuring proton mass transport, and the gas phase supplied by a back flow of their respective substrates, i.e. H_2 or O_2. However, this proof-of-concept setup could lead to a significant performance drop linked to possible O_2 crossover to the complex 1-based anode. This was minimized via N_2 bubbling in the electrolyte. The distance between cathode and anode was set to 0.5 cm. Figure 8 displays the polarization and power curves recorded by scanning the cell voltage from open circuit voltage (OCV) down to 0.25 V at a scan rate of 0.5 mV s^{-1} using the anode sample characterized in Figure 7. The membrane-less fuel cell device based on the complex 1 as anode catalyst delivers a maximum power density of 31 μW cm^{-2} at 0.60 V and is characterized by an OCV of 0.9 V. Similar results were obtained for three other fuel cells devices with power output ranging from 10 to 31 μW cm^{-2}. For comparison, catalyst-free carbon black anode and Pt/C-based GDE were also integrated as anodes in the same fuel cell setup, resulting in OCVs of 0.68 V and 1.06 V and power output of 6 ± 1 and 85 ± 6 μW cm^{-2} at 0.6 V cell voltage, respectively. The four membrane-less fuel cell devices prepared with the complex 1 anode catalyst all display performances significantly better to those with only carbon black at the anode, as far as both OCV and power output is concerned. When compared to Pt/C-based GDE, the OCV observed for complex 1/GDE are very similar with a power output of around 30% of that of Pt/C GDE.

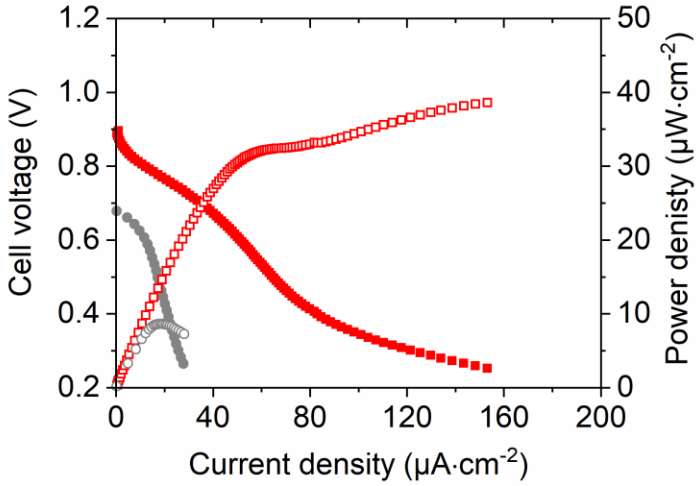

Figure 8. Polarization (filled marks) and power (empty marks) curves for Pt/C | aq. KPF_6| complex **1**/C (red marks) and Pt/C | aq. KPF_6| C (no anode catalyst, grey marks) membrane-less fuel cell device; anode and cathode were fed with pure H_2 and O_2 (1 atm , 10 ml min^{-1}, 20°C) and the electrolyte was degassed 0.1 M KPF_6 adjusted to pH = 5.6.

This membrane-less fuel cell device is the first example using a mimic of the active site of [FeFe]-hydrogenase as the anode catalyst. Although not as efficient as the Pt-free membrane-less H_2/O_2 fuel cell reported by some of us based on an arginine derivative of the nickel bisdiphosphine catalysts that displays 150 $\mu W.cm^{-2}$ at 0.2V,[63] this new device already outperforms previously-designed zero-gap fuel cells integrating mimics of the active sites of [NiFe]-hydrogenases delivering 11 $\mu W\ cm^{-2}$ with an OCV of 0.3 V[12] and 25 $\mu W\ cm^{-2}$ with an OCV of 0.42 V[64] and including noble metals as part of the catalysts' composition. The low power densities observed in these proof-of concept devices can however be improved by several orders of magnitude through optimization of the composition and structuration of the electrodes, as demonstrated for zero-gap Pt-free PEM fuel cells based on immobilized DuBois nickel bisdiphosphine catalysts with a 2 orders of magnitude improvement,[62,65,66] or biofuels cells based on natural hydrogenases that were first reported with a 5$\mu W.cm^{-2}$ power density[67] and have now reached over 8 $mA.cm^{-2}$.[68,69]

Conclusion

After two decades of biomimicry of the active site of [FeFe]-hydrogenase, a subtle modification of the bridging azadithiolate ligand allowed us to design the first diiron mimic with hydrogen

oxidation activity, as a result of (i) a preferred conformation positioning the nitrogen lone pair toward the H_2 binding site and (ii) an increased basicity of the amine function due to hindered delocalization of the nitrogen lone-pair allowing for heterolytic H_2 cleavage. This is therefore the first diiron complex able to activate H_2 via a mechanism reminiscent of that followed by the enzyme. This system however uses oxidation states of the active site lower by one unit to activate both protons and H_2. The lack of reversibility for bidirectional catalysis can be explained by the existence of a potential window at which an intermediate of both HER and HOR cycles predominates and the catalytic bias towards HER over HOR could be rationalized based on the kinetic barriers required to activate protons and H_2, respectively. Structural variations, such as modifications of the iron ligand sets and modifications of the substituents in the *ortho* position of the aryl-ADT ligand could allow to tune the potentials of the redox processes and the kinetics for substrates binding, so as to obtain reversible bidirectional catalytic behavior or modify the catalytic bias. Noteworthy, this system showed quite high stability with ~200 turnovers under bulk conditions. It can therefore be considered as a novel blueprint for the preparation of cost-effective HOR catalysts made of one of the most abundant transition metals and is a promising candidate to be integrated at the anode of hybrid biofuel cells.[62]

Experimental section.

Materials

Complex **1** was synthesized according to previously reported procedure.[23] Syntheses of all the complexes were performed either under anaerobic atmosphere or in an Ar Glove Box from MBRAUN. Complex **1** was synthesized using standard Schlenk techniques. 2-Ethylaniline and the solvents were used fresh after distillation, purchased from Merck. Thionyl chloride ($SOCl_2$) was purchased from Spectrochem Pvt. Ltd. (India). *p*-formaldehyde, superhydride ($Li[HBEt_3]$, 1 M in THF), N,N-diisopropylethylamine, malonic acid and bis(cyclopentadienyl)cobalt(II) were purchased from Sigma-Aldrich chemicals Pvt. Ltd., and anhydrous Na_2SO_4 was purchased from Merck Specialities, Pvt. Ltd. (India). During electrochemistry the solvent (acetonitrile) was used after distillation with proper drying agent. Silica (60-120 mesh), for column chromatography, was purchased from SISCO Pvt. Ltd. (India). Edge Plane Graphite (EPG) discs were purchased from Pine Instruments. Glassy carbon plate (1 mm thick, type1) was purchased from Alfa Aesar. The FT-IR data are measured on the Perkin-Elmer FTIR Frontier instrument. The CaF_2 windows

for FTIR spectroscopy were purchased from Sigma Aldrich. The anaerobic setup for FTIR spectroscopy was purchased from PerkinElmer. All the NMR spectra were recorded on Bruker DPX-400 or DPX-500 spectrometers at room temperature. The mass spectra are recorded on an QTOF Micro YA263 instrument. UV-Vis absorption data were recorded in an Agilent technologies spectrophotometer model 8453 fitted with a diode-array detector. Mössbauer spectra were recorded in an alternating constant WissEl Mössbauer spectrometer, which consists of an MR 360 drive unit, an MVT 1000 velocity transducer, and an LND-45431 proportional counter mounted on an MB-600 Mössbauer bench with cryostat stand. The system was operated in a horizontal transmission geometry with source (^{57}Co in Rh-matrix), absorber and detector in a linear arrangement. The temperature was controlled and maintained using MBBC-N20106 Mössbauer cryostat for liquid nitrogen connected with Lake Shore-325 temperature controller unit. Measurements were performed at 90K. Data acquisition was performed using a 512 channel analyzer. Isomer shifts were referenced versus α-iron metal foil at the same temperature. The simulation of experimental data was performed using the Normos-A Mössbauer Fit programmes Site and Dist.

For fuel-cell measurements, commercial carbon black Vulcan VXC72 was obtained from Cabot and used as received. Gas diffusion layer (GDL) Sigracet 39-BC with hydrophobic treatment (5 wt % PTFE) and microporous layer was purchased from SGL Carbon GmbH (Germany). Platinum gas diffusion electrodes with 0.5 mg_{Pt} cm^{-2} (60% Pt on Vulcan carbon support) were purchased from FuelCellStore. Oxygen gas and hydrogen gas (Air Liquide ultrapure quality) were of 99.995% and 99.999% purity, respectively.

UV-Vis Spectroscopy

UV-Vis absorption data were recorded in an Agilent technologies spectrophotometer model 8453 fitted with a diode-array detector. During the experiments, anaerobic cuvettes (path length 1 cm) with rubber septum were used.

NMR Spectroscopy

All the NMR spectra were recorded on Bruker DPX-400 or DPX-500 spectrometers at room temperature.

FTIR Spectroscopy

FT-IR spectra of the complexes are recorded by a Perkin-Elmer Frontier FT-IR spectrometer in a CaF_2 window. ACN solution of the complex **1** (500 μL; 2 mM) was prepared in a vial, and reduced by using fifty equivalents of cobaltocene inside the glove box, then 50 equivalents of malonic acid were added to it. The sample was injected in the anaerobic FTIR setup and tightly sealed. The cell was taken out from the box for data collection.

Time-resolved FTIR spectroscopy

Solutions of complex **1** (0.0015 mmol, 0.6 mL), $CoCp_2$ (Sigma Aldrich, 100 equivalents, 3 mL) and malonic acid (Sigma Aldrich, 25 equivalents, 3 mL) in acetonitrile were prepared under argon atmosphere inside Unilab (MBraun) glove box. Acetonitrile (UVASOL, Sigma Aldrich) was dried by refluxing in CaH_2 and degassed using freeze-pump-thaw technique. The three solutions were transferred from the glove box to the rapid mixing accessory in gas-tight transfer syringes. Malonic acid solution was mounted on the first drive syringe. Solutions of complex **1** and $CoCp_2$ were mounted on the second drive syringe and mixed by pushing the liquid from the drive to the transfer syringe and back three times. Stopped-flow experiments were initiated immediately after mixing of the solutions containing complex **1** and $CoCp_2$. The experiments were conducted on SFA-20 rapid mixing accessory provided by TgK Scientific. The optical cell incorporated in the rapid mixing accessory consisted of two CaF_2 windows and had the optical path length of 0.5 mm. The nominal dead time of the stopped-flow setup was <8 ms. Rapid scan FTIR measurements were performed on a Bruker Vertex 70v spectrometer with a MCT detector. The wavenumber region 1000-4000 cm^{-1} was scanned every 50 ms with the resolution of 2 cm^{-1}.

Mössbauer Spectroscopy

ACN solutions of the complex **1** (150 μL; 40 mM) was prepared inside the glove box, and the $Fe^{I}Fe^{I}$ state data was collected. Then the sample was reduced using fifty equivalents of cobaltocene and fifty equivalents of malonic acid was added to it inside a glove box. With this sample the data was collected for the intermediate. In each of the cases mentioned above, 150 μL sample was taken in a custom-made Nylon capsule, froze with liquid N_2 inside the glove box, and immediately taken out, attached to the sample holder (immersed into liquid N_2) using a screw joint, and inserted into the cryostat maintained at 90K for data collection (Figure S1).

EPR Spectroscopy

The X-band EPR spectrum of **1H** was recorded with a Bruker EMX X-band spectrometer operating at a field modulation of 100 kHz with a modulation amplitude of 10 G and microwave radiation power of 1.03 mW at 77 K.

Electrochemical Measurements

Cyclic Voltammetry: All electrochemical experiments were performed using a CH Instruments (model CHI 710D Bi-potentiostat Electrochemical Analyzer). Reference electrodes, Teflon® plate material evaluating cell (ALS Japan) were purchased from CH Instruments. A Pt wire electrode was used as a counter electrode. The measurements were made against a leak proof Ag/AgCl aqueous reference electrode (satd. KCl). Anaerobic experiment was performed within a 5 neck S3 water jacket electrochemical cell brought from PINE Instruments or in a 4-neck custom made electrochemical cell by thoroughly degassing the whole set up with Ar gas.

Preparation of modified Edge Plane Graphite electrode: The edge plane graphite (EPG) electrodes were freshly polished and cleaned with polishing kit before each single experimental use. A 200 μL portion of a dilute solution (~1 mM, in $CHCl_3$) was uniformly drop casted on cleaned EPG disc (3.5 mm diameter) fitted within a shaft. After $CHCl_3$ evaporation, the surface was washed with $CHCl_3$ thoroughly and then ethanol to remove any loosely bound catalyst on the surface and washed with triple distilled water.

Aqueous electrochemical measurements: All the electrochemical experiments were performed using a CH Instruments (model CHI 710D Electrochemical Analyzer). Reference electrodes, Pt counter electrodes were purchased from CH Instruments. The rotating ring disk electrochemical (RRDE) set up from Pine Research Instrumentation (E6 series Change Disk tips with AFE6M rotor) was used to obtain the RDE and LSV data on modified EPGs. A Pt wire was used as a counter electrode. The measurements were made against an Ag/AgCl aqueous leak proof reference electrode (satd. KCl). Anaerobic CV experiment was performed within a 5 neck S3 water jacket electrochemical cell brought from PINE Instruments by thoroughly degassing the whole set up with Ar gas. The cyclic and rotating disk electrode voltammograms were recorded

in 0.1 M KPF_6 water solution with all of the complexes adsorbed onto the EPG disc held within a shaft (Pine Instruments, AFE6MB).

Non-aqueous electrochemical measurements*:* Electrochemical measurements were carried out in MeCN solution (Merck, HPLC gradient grade 99.99%), 0.1 M Bu_4NClO_4 (Sigma-Aldrich, for electrochemical analysis ≥99%, used as received), under argon (cyclic voltammetry, CV) or nitrogen (controlled potential electrolysis, CPE) atmosphere at 20-25 °C using a CH Instruments (model CHI 710D Electrochemical Analyzer). For CV experiments, a 4-neck custom made electrochemical cell was used. Potentials were referred to an Ag/AgCl (satd. KCl) reference electrode in MeCN + 0.1 M Bu_4NClO_4 and measured potentials were calibrated through the use of an internal Fc/Fc^+ standard. A glassy carbon electrode (CV, LSV) and a glassy carbon plate electrode (CPE) were used as a working electrode. The auxiliary electrode was a Pt wire in MeCN + 0.1 M Bu_4NClO_4 solution. Bulk electrolyses and coulometry were carried out in a 4-neck custom made electrochemical cell using a glassy carbon plate electrode. The reference electrode was externally calibrated vs Fc^+/Fc. The electrochemistry was performed after saturating the acetonitrile solution with H_2 gas (45 mins purging).

H_2 concentration dependence using mass flow meter: The H_2 concentration dependence experiments in aqueous medium (heterogeneous conditions) were done using Mani-Flow (BRONKHORST) gas flow meter, which was connected with a digital Power Supply Flow Indicator Controller (PSFIC) (EUTECH SYSTEMS). Using PSFIC one can control the mass flow rate of the gas. In this experiment we used two different digital gas flow meters with full setup (One for H_2 gas control and another for Argon gas control). The outlet from these two flow meters were put into a closed vessel through a rubber septum, in which two gases are mixed and form a homogeneous gas mixture. Another outlet of this closed vessel was connected to the electrochemical cell. During the H_2 concentration dependence experiment different types of H_2/Ar gas mixture were used. During the experiments, each time the gas mixture was purged for 45 mins into the solution and then the data was recorded. During homogeneous study, the H_2 partial pressure dependence experiments were done by using CVG Technocrafts India mass flow meter purchased from Chemix. Mass flow rate of the gases were controlled manually during the experiments using regulator. Instead of digital flow meter the other procedures were same as heterogeneous study.

Bulk electrolysis and NMR spectroscopy: The BE experiment was done in a custom made 4 neck electrochemical cell with glassy carbon (2×2.25 cm^2) working electrode. After saturating the acetonitrile-d_3 solution (containing 0.5 mM complex **1** and 10 M diisopropylethylamine) with H_2 gas the BE experiment was performed. After different time interval of BE, 450 µL solution was syringe out anaerobically from the electrochemical cell and took into an NMR tube; after performing ^1H NMR, the solution was put back into the electrochemical cell anaerobically and then again performed the BE experiment. During the experiments occasionally H_2 gas was purging (after 90 mins and 240 mins). The amount of ammonium produced was quantified from the integration values of the new peak which is generating and increasing with time at 7.59 ppm. We consider the integration of the $-CH_2-$ peak at 3.78 ppm is 1.

The faradic yield (FY) was determined by the equation (iv) and reported in Table S1.

FY = 2 × amount of ammonium measured/(Charge/F) = 2F × amount of ammonium measured/Charge (iii)

Membrane-less fuel cell measurements

Preparation and characterization of the electrodes

Catalyst ink was prepared using the following formulation: 100 µl of a 2 mg ml^{-1} dispersion of Vulcan VXC72 in CH_2Cl_2 were mixed with 50 µl of a solution of **1** in CH_2Cl_2 (4 mM). This formulation corresponds to a Vulcan VXC72-to- **Fe2** mass ratio of 2:1. Then, an aliquot of 50 µl of the catalyst ink was deposited on the microporous layer of a 1.13 cm^2 GDL to reach a loading of 30 µg cm^{-2} of **1** (0.06 µmol cm^{-2} or 60 nmol cm^{-2}). The working gas diffusion electrodes (GDEs) with the deposited catalyst layer was used in a three-electrode cell configuration described elsewhere[60] and in the membrane-less fuel cell configuration (Figure S10). The blank working electrodes used in the experimental setups consisted of GDEs with 0.09 mg_{Vulcan} cm^{-2}.

Membrane-less fuel cell setup

The membrane-less fuel cell experimental setup is show in Figure S10 and consists of two half-cell holders with the GDEs placed face-to-face in a special glass cell filled with degassed electrolyte. The cathode is a commercial GDE with 0.5 $mg_{Pt}\cdot cm^{-2}$. Polarization curves were recorded by scanning the cell voltage from open circuit voltage (OCV) down to 0.25 V at a scan

rate of 0.5 mV s^{-1} and 25°C, under a back-flow of H_2 (1 atm, 10 ml min^{-1}) at the anode and a back-flow of O_2 (1 atm, 10 ml min^{-1}) at the cathode.

Computational Details

The geometries were optimized in Gaussian 16 software[48] using the B3LYP functional,[49,50] 6-311g* basis set and PCM-dispersion model. Frequency calculations were performed to ensure the presence of a minimum. The single point calculations were calculated using the same functional but a 6-311+g* basis set and 10^{-10} convergence criteria. Reduction potentials were calculated vs Fc/Fc^+ and 271 kCal/mol for proton.[70]

Associated Content

Supporting Information

Detailed experimental conditions, preparation and characterization of electrodes, fuel cell experimental setup and other addition information are available free of charge in the online version of the paper. Correspondence and requests for materials should be addressed to V.A. and A.D.

Acknowledgments

This work was supported by the Indo-French Center for the Promotion of Advanced Research (IFCPAR/CEFIPRA grant n° 5405-1), the French National Research Agency (Labex program, ARCANE, Graduate school of Chemistry, Biology and Health of Univ. Grenoble Alpes, CBH-EUR-GS, ANR-17-EURE-0003) and Department of Science and Technology, India, Grant DST/TMD/HFC/2K18/90. M.E.A. and A. N. acknowledgesCSIR (SRF) and DST-Inspire for the fellowship, respectively.

Notes

The authors declare no competing financial interests.

References:

(1) Fujishima, A.; Honda, K. Electrochemical Photolysis of Water at a Semiconductor Electrode. *Nature* **1972**, *238*, 37-38.

(2) Bard, A. J.; Fox, M. A. Artificial Photosynthesis: Solar Splitting of Water to Hydrogen and Oxygen. *Acc. Chem. Res.* **1995**, *28*, 141-145.

(3) Heller, A. Hydrogen-Evolving Solar Cells. *Science* **1984**, *223*, 1141.

(4) Maeda, K.; Domen, K. Photocatalytic Water Splitting: Recent Progress and Future Challenges. *The Journal of Physical Chemistry Letters* **2010**, *1*, 2655-2661.

(5) Kudo, A.; Miseki, Y. Heterogeneous photocatalyst materials for water splitting. *Chem. Soc. Rev.* **2009**, *38*, 253-278.

(6) Maeda, K.; Domen, K. New Non-Oxide Photocatalysts Designed for Overall Water Splitting under Visible Light. *The Journal of Physical Chemistry C* **2007**, *111*, 7851-7861.

(7) Ardo, S.; Fernandez Rivas, D.; Modestino, M. A.; Schulze Greiving, V.; Abdi, F. F.; Alarcon Llado, E.; Artero, V.; Ayers, K.; Battaglia, C.; Becker, J.-P.; Bederak, D.; Berger, A.; Buda, F.; Chinello, E.; Dam, B.; Di Palma, V.; Edvinsson, T.; Fujii, K.; Gardeniers, H.; Geerlings, H.; H. Hashemi, S. M.; Haussener, S.; Houle, F.; Huskens, J.; James, B. D.; Konrad, K.; Kudo, A.; Kunturu, P. P.; Lohse, D.; Mei, B.; Miller, E. L.; Moore, G. F.; Muller, J.; Orchard, K. L.; Rosser, T. E.; Saadi, F. H.; Schüttauf, J.-W.; Seger, B.; Sheehan, S. W.; Smith, W. A.; Spurgeon, J.; Tang, M. H.; van de Krol, R.; Vesborg, P. C. K.; Westerik, P. Pathways to electrochemical solar-hydrogen technologies. *Energy Environ. Sci.* **2018**, *11*, 2768-2783.

(8) Kibsgaard, J.; Chorkendorff, I. Considerations for the scaling-up of water splitting catalysts. *Nature Energy* **2019**, *4*, 430-433.

(9) Luan, P.; Zhang, J. Stepping Towards Solar Water Splitting: Recent Progress in Bismuth Vanadate Photoanodes. *ChemElectroChem*. **2019**, *6*, 3227-3243.

(10) Diat, O.; Gebel, G. Proton channels. *Nature Materials* **2008**, *7*, 13.

(11) Cracknell, J. A.; Vincent, K. A.; Armstrong, F. A. Enzymes as Working or Inspirational Electrocatalysts for Fuel Cells and Electrolysis. *Chemical Reviews* **2008**, *108*, 2439-2461.

(12) Matsumoto, T.; Kim, K.; Ogo, S. Molecular Catalysis in a Fuel Cell. *Angew. Chem. Int. Ed.* **2011**, *50*, 11202-11205.

(13) Beni, G.; Schiavone, L. M.; Shay, J. L.; Dautremont-Smith, W. C.; Schneider, B. S. Electrocatalytic oxygen evolution on reactively sputtered electrochromic iridium oxide films. *Nature* **1979**, *282*, 281-283.

(14) Vincent, K. A.; Cracknell, J. A.; Clark, J. R.; Ludwig, M.; Lenz, O.; Friedrich, B.; Armstrong, F. A. Electricity from low-level H2 in still air – an ultimate test for an oxygen tolerant hydrogenase. *Chem. Commun.* **2006**, 5033-5035.

(15) Wait, A. F.; Parkin, A.; Morley, G. M.; dos Santos, L.; Armstrong, F. A. Characteristics of Enzyme-Based Hydrogen Fuel Cells Using an Oxygen-Tolerant Hydrogenase as the Anodic Catalyst. *The Journal of Physical Chemistry C* **2010**, *114*, 12003-12009.

(16) Rüdiger, O.; Gutiérrez-Sánchez, C.; Olea, D.; Pereira, I. A. C.; Vélez, M.; Fernández, V. M.; De Lacey, A. L. Enzymatic Anodes for Hydrogen Fuel Cells based on Covalent Attachment of Ni-Fe Hydrogenases and Direct Electron Transfer to SAM-Modified Gold Electrodes. *Electroanalysis* **2010**, *22*, 776-783.

(17) Fasano, A.; Land, H.; Fourmond, V.; Berggren, G.; Léger, C. Reversible or Irreversible Catalysis of H+/H2 Conversion by FeFe Hydrogenases. *J. Am. Chem. Soc.* **2021**, *143*, 48, 20320–20325.

(18) Land, H.; Sekretareva, A.; Huang, P.; Redman, H. J.; Németh, B.; Polidori, N.; Mészáros, L. S.; Senger, M.; Stripp, S. T.; Berggren, G. Characterization of a putative sensory [FeFe]-hydrogenase provides new insight into the role of the active site architecture. *Chem. Sci.* **2020**, *11*, 12789-12801.

(19) Stiebritz, M. T.; Reiher, M. Hydrogenases and oxygen. *Chem. Sci.* **2012**, *3*, 1739-1751.

(20) Lambertz, C.; Leidel, N.; Havelius, K. G. V.; Noth, J.; Chernev, P.; Winkler, M.; Happe, T.; Haumann, M. O2 Reactions at the Six-iron Active Site (H-cluster) in [FeFe]-Hydrogenase. *J. Biol. Chem.* **2011**, *286*, 40614-40623.

(21) Lubitz, W.; Ogata, H.; Rüdiger, O.; Reijerse, E. Hydrogenases. *Chem. Rev.* **2014**, *114*, 4081-4148.

(22) Seh, Z. W.; Kibsgaard, J.; Dickens, C. F.; Chorkendorff, I.; Nørskov, J. K.; Jaramillo, T. F. Combining theory and experiment in electrocatalysis: Insights into materials design. *Science* **2017**, *355*, eaad4998.

(23) Ahmed, M. E.; Dey, S.; Darensbourg, M. Y.; Dey, A. Oxygen-Tolerant H2 Production by [FeFe]-H2ase Active Site Mimics Aided by Second Sphere Proton Shuttle. *J. Am. Chem. Soc.* **2018**, *140*, 12457-12468.

(24) Wakerley, D. W.; Reisner, E. Oxygen-tolerant proton reduction catalysis: much O2 about nothing? *Energy Environ. Sci.* **2015**, *8*, 2283-2295.

(25) Mondal, B.; Dey, A. Development of air-stable hydrogen evolution catalysts. *Chem. Commun.* **2017**, *53*, 7707-7715.

(26) Dutta, A.; Appel, A. M.; Shaw, W. J. Designing electrochemically reversible H2 oxidation and production catalysts. *Nat. Rev. Chem.* **2018**, *2*, 244-252.

(27) Smith, S. E.; Yang, J. Y.; DuBois, D. L.; Bullock, R. M. Reversible Electrocatalytic Production and Oxidation of Hydrogen at Low Overpotentials by a Functional Hydrogenase Mimic. *Angew. Chem. Int. Ed.* **2012**, *51*, 3152-3155.

(28) DuBois, D. L. Development of Molecular Electrocatalysts for Energy Storage. *Inorg. Chem.* **2014**, *53*, 3935-3960.

(29) Wilson, A. D.; Newell, R. H.; McNevin, M. J.; Muckerman, J. T.; Rakowski DuBois, M.; DuBois, D. L. Hydrogen Oxidation and Production Using Nickel-Based Molecular Catalysts with Positioned Proton Relays. *J. Am. Chem. Soc.* **2006**, *128*, 358-366.

(30) Wang, N.; Wang, M.; Wang, Y.; Zheng, D.; Han, H.; Ahlquist, M. S. G.; Sun, L. Catalytic Activation of H2 under Mild Conditions by an [FeFe]-Hydrogenase Model via an Active μ-Hydride Species. *J. Am. Chem. Soc.* **2013**, *135*, 13688-13691.

(31) Camara, J. M.; Rauchfuss, T. B. Combining acid–base, redox and substrate binding functionalities to give a complete model for the [FeFe]-hydrogenase. *Nat. Chem.* **2012**, *4*, 26-30.

(32) Dey, S.; Rana, A.; Dey, S. G.; Dey, A. Electrochemical Hydrogen Production in Acidic Water by an Azadithiolate Bridged Synthetic Hydrogenese Mimic: Role of Aqueous Solvation in Lowering Overpotential. *ACS Catal.* **2013**, *3*, 429-436.

(33) Ahmed, M. E.; Dey, S.; Mondal, B.; Dey, A. H2 evolution catalyzed by a FeFe-hydrogenase synthetic model covalently attached to graphite surfaces. *Chem. Commun.*, **2017**,*53*, 8188-8191.

(34) Dey, S.; Rana, A.; Crouthers, D.; Mondal, B.; Das, P. K.; Darensbourg, M. Y.; Dey, A. Electrocatalytic O2 Reduction by [Fe-Fe]-Hydrogenase Active Site Models. *J. Am. Chem. Soc.* **2014**, *136*, 8847-8850.

(35) Roy, S.; Sharma, B.; Pécaut, J.; Simon, P.; Fontecave, M.; Tran, P. D.; Derat, E.; Artero, V. Molecular Cobalt Complexes with Pendant Amines for Selective Electrocatalytic Reduction of Carbon Dioxide to Formic Acid. *J. Am. Chem. Soc.* **2017**, *139*, 3685-3696.

(36) Ahmed, M. E.; Rana, A.; Saha, R.; Dey, S.; Dey, A. Homogeneous Electrochemical Reduction of CO2 to CO by a Cobalt Pyridine Thiolate Complex. *Inorg. Chem.* **2020**, *59*, 5292-5302.

(37) Kelly-Rowley, A. M.; Lynch, V. M.; Anslyn, E. V. Molecular Recognition of Enolates of Active Methylene Compounds in Acetonitrile. The Interplay between Complementarity and Basicity and the Use of Hydrogen Bonding to Lower Guest pKas. *J. Am. Chem. Soc.* **1995**, *117*, 3438-3447.

(38) Fourmond, V.; Jacques, P.-A.; Fontecave, M.; Artero, V. H2 Evolution and Molecular Electrocatalysts: Determination of Overpotentials and Effect of Homoconjugation. *Inorg. Chem.* **2010**, *49*, 10338-10347.

(39) Yang, J. Y.; Smith, S. E.; Liu, T.; Dougherty, W. G.; Hoffert, W. A.; Kassel, W. S.; DuBois, M. R.; DuBois, D. L.; Bullock, R. M. Two Pathways for Electrocatalytic Oxidation of Hydrogen by a Nickel Bis(diphosphine) Complex with Pendant Amines in the Second Coordination Sphere. *J. Am. Chem. Soc.* **2013**, *135*, 9700-9712.

(40) Tard, C.; Pickett, C. J. Structural and Functional Analogues of the Active Sites of the [Fe]-, [NiFe]-, and [FeFe]-Hydrogenases. *Chemical Reviews* **2009**, *109*, 2245-2274.

(41) Adamska-Venkatesh, A.; Roy, S.; Siebel, J. F.; Simmons, T. R.; Fontecave, M.; Artero, V.; Reijerse, E.; Lubitz, W. Spectroscopic Characterization of the Bridging Amine in the Active Site of [FeFe] Hydrogenase Using Isotopologues of the H-Cluster. *J. Am. Chem. Soc.* **2015**, *137*, 12744-12747.

(42) Rodríguez-Maciá, P.; Pawlak, K.; Rüdiger, O.; Reijerse, E. J.; Lubitz, W.; Birrell, J. A. Intercluster Redox Coupling Influences Protonation at the H-cluster in [FeFe] Hydrogenases. *J. Am. Chem. Soc.* **2017**, *139*, 15122-15134.

(43) Aster, A.; Wang, S.; Mirmohades, M.; Esmieu, C.; Berggren, G.; Hammarström, L.; Lomoth, R. Metal vs. ligand protonation and the alleged proton-shuttling role of the azadithiolate ligand in catalytic H2 formation with FeFe hydrogenase model complexes. *Chem. Sci.* **2019**, *10*, 5582-5588.

(44) Wright, J. A.; Webster, L.; Jablonskytė, A.; Woi, P. M.; Ibrahim, S. K.; Pickett, C. J. Protonation of [FeFe]-hydrogenase sub-site analogues: revealing mechanism using FTIR stopped-flow techniques. *Faraday Discuss.* **2011**, *148*, 359-371.

(45) Song, L.-C.; Yang, Z.-Y.; Bian, H.-Z.; Hu, Q.-M. Novel Single and Double Diiron Oxadithiolates as Models for the Active Site of [Fe]-Only Hydrogenases. *Organometallics* **2004**, *23*, 3082-3084.

(46) Apfel, U.-P.; Troegel, D.; Halpin, Y.; Tschierlei, S.; Uhlemann, U.; Görls, H.; Schmitt, M.; Popp, J.; Dunne, P.; Venkatesan, M.; Coey, M.; Rudolph, M.; Vos, J. G.; Tacke, R.; Weigand, W. Models for the Active Site in [FeFe] Hydrogenase with Iron-Bound Ligands Derived from Bis-, Tris-, and Tetrakis(mercaptomethyl)silanes. *Inorg. Chem.* **2010**, *49*, 10117-10132.

(47) Tschierlei, S.; Ott, S.; Lomoth, R. Spectroscopically characterized intermediates of catalytic H2 formation by [FeFe] hydrogenase models. *Energy Environ. Sci.* **2011**, *4*, 2340-2352.

(48) MJ, F. . Gaussian 03, C.02; Gaussian, Inc.: Wallingford,

CT, **2004**.

(49) Perdew, J. P. Density-functional approximation for the correlation energy of the inhomogeneous electron gas. *Phys. Rev. B* **1986**, *33*, 8822-8824.

(50) Becke, A. D. Density-functional exchange-energy approximation with correct asymptotic behavior. *Phys. Rev. A* **1988**, *38*, 3098-3100.

(51) Rana, A.; Kumar Das, P.; Mondal, B.; Dey, S.; Crouthers, D.; Dey, A. Investigation of Bridgehead Effects on Reduction Potential in Alkyl and Aryl Azadithiolate-Bridged (μ-SCH2XCH2S) [Fe(CO)3]2 Synthetic Analogues of [FeFe]-H2ase Active Site. *European Journal of Inorganic Chemistry* **2018**, *2018*, 3633-3643.

(52) Capon, J.-F.; Gloaguen, F.; Pétillon, F. Y.; Schollhammer, P.; Talarmin, J. Electron and proton transfers at diiron dithiolate sites relevant to the catalysis of proton reduction by the [FeFe]-hydrogenases. *Coord. Chem. Rev.* **2009**, *253*, 1476-1494.

(53) Bourrez, M.; Steinmetz, R.; Gloaguen, F. Mechanistic Insights into the Catalysis of Electrochemical Proton Reduction by a Diiron Azadithiolate Complex. *Inorg. Chem.* **2014**, *53*, 10667-10673.

(54) Reiss, H.; Heller, A. The absolute potential of the standard hydrogen electrode: a new estimate. *The Journal of Physical Chemistry* **1985**, *89*, 4207-4213.

(55) Ezzaher, S.; Capon, J.-F.; Gloaguen, F.; Pétillon, F. Y.; Schollhammer, P.; Talarmin, J.; Pichon, R.; Kervarec, N. Evidence for the Formation of Terminal Hydrides by Protonation of an Asymmetric Iron Hydrogenase Active Site Mimic. *Inorg. Chem.* **2007**, *46*, 3426-3428.

(56) Amanullah, S.; Saha, P.; Nayek, A.; Ahmed, M. E.; Dey, A. Biochemical and artificial pathways for the reduction of carbon dioxide, nitrite and the competing proton reduction: effect of 2nd sphere interactions in catalysis. *Chem. Soc. Rev.* **2021**, *50*, 3755-3823.

(57) Senger, M.; Mebs, S.; Duan, J.; Shulenina, O.; Laun, K.; Kertess, L.; Wittkamp, F.; Apfel, U.-P.; Happe, T.; Winkler, M.; Haumann, M.; Stripp, S. T. Protonation/reduction dynamics at the [4Fe–4S] cluster of the hydrogen-forming cofactor in [FeFe]-hydrogenases. *Phys. Chem. Chem. Phys.* **2018**, *20*, 3128-3140.

(58) Sommer, C.; Adamska-Venkatesh, A.; Pawlak, K.; Birrell, J. A.; Rüdiger, O.; Reijerse, E. J.; Lubitz, W. Proton Coupled Electronic Rearrangement within the H-Cluster as an Essential Step in the Catalytic Cycle of [FeFe] Hydrogenases. *J. Am. Chem. Soc.* **2017**, *139*, 1440-1443.

(59) Kleinhaus, J. T.; Wittkamp, F.; Yadav, S.; Siegmund, D.; Apfel, U.-P. [FeFe]-Hydrogenases: maturation and reactivity of enzymatic systems and overview of biomimetic models. *Chem. Soc. Rev.* **2021**, *50*, 1668-1784.

(60) Le Goff, A.; Artero, V.; Jousselme, B.; Tran, P. D.; Guillet, N.; Métayé, R.; Fihri, A.; Palacin, S.; Fontecave, M. From Hydrogenases to Noble Metal–Free Catalytic Nanomaterials for H2 Production and Uptake. *Science* **2009**, *326*, 1384-1387.

(61) Huan, T. N.; Jane, R. T.; Benayad, A.; Guetaz, L.; Tran, P. D.; Artero, V. Bio-inspired noble metal-free nanomaterials approaching platinum performances for H2 evolution and uptake. *Energy Environ. Sci.* **2016**, *9*, 940-947.

(62) Gentil, S.; Lalaoui, N.; Dutta, A.; Nedellec, Y.; Cosnier, S.; Shaw, W. J.; Artero, V.; Le Goff, A. Carbon-Nanotube-Supported Bio-Inspired Nickel Catalyst and Its Integration in Hybrid Hydrogen/Air Fuel Cells. *Angew. Chem. Int. Ed.* **2017**, *56*, 1845-1849.

(63) Gentil, S.; Molloy, J. K.; Carrière, M.; Hobballah, A.; Dutta, A.; Cosnier, S.; Shaw, W. J.; Gellon, G.; Belle, C.; Artero, V.; Thomas, F.; Le Goff, A. A Nanotube-Supported Dicopper Complex Enhances Pt-free Molecular H2/Air Fuel Cells. *Joule*, **2019**, *3*, 2020-2029.

(64) Matsumoto, T.; Kim, K.; Nakai, H.; Hibino, T.; Ogo, S. Organometallic Catalysts for Use in a Fuel Cell. *ChemCatChem* **2013**, *5*, 1368-1373.

(65) Tran, P. D.; Morozan, A.; Archambault, S.; Heidkamp, J.; Chenevier, P.; Dau, H.; Fontecave, M.; Martinent, A.; Jousselme, B.; Artero, V. A noble metal-free proton-exchange membrane fuel cell based on bio-inspired molecular catalysts. *Chem. Sci.* **2015**, *6*, 2050-2053.

(66) Coutard, N.; Reuillard, B.; Huan, T. N.; Valentino, F.; Jane, R. T.; Gentil, S.; Andreiadis, E. S.; Le Goff, A.; Asset, T.; Maillard, F.; Jousselme, B.; Morozan, A.; Lyonnard, S.; Artero, V.; Chenevier, P. Impact of ionomer structuration on the performance of bio-inspired noble-metal-free fuel cell anodes. *Chem Catalysis* **2021**, *1*, 88-105.

(67) Vincent, K. A.; Cracknell, J. A.; Lenz, O.; Zebger, I.; Friedrich, B.; Armstrong, F. A. Electrocatalytic hydrogen oxidation by an enzyme at high carbon monoxide or oxygen levels. *Proceedings of the National Academy of Sciences of the United States of America* **2005**, *102*, 16951-16954.

(68) So, K.; Kitazumi, Y.; Shirai, O.; Nishikawa, K.; Higuchi, Y.; Kano, K. Direct electron transfer-type dual gas diffusion H2/O2 biofuel cells. *J. Mater. Chem. A* **2016**, *4*, 8742-8749.

(69) Xiao, X.; Xia, H.-q.; Wu, R.; Bai, L.; Yan, L.; Magner, E.; Cosnier, S.; Lojou, E.; Zhu, Z.; Liu, A. Tackling the Challenges of Enzymatic (Bio)Fuel Cells. *Chemical Reviews* **2019**, *119*, 9509-9558.

(70) Kelly, C. P.; Cramer, C. J.; Truhlar, D. G. Aqueous Solvation Free Energies of Ions and Ion−Water Clusters Based on an Accurate Value for the Absolute Aqueous Solvation Free Energy of the Proton. *J. Phys. Chem. B* **2006**, *110*, 16066-16081.